Am J Cancer Res 2021;11(4):1586-1599
www.ajcr.us /ISSN:2156-6976/ajcr0127905

Original Article

ImmunoPET of the differential expression of CD146 in breast cancer

Carolina A Ferreira[1*], Lei Kang[2,3*], Cuicui Li[2], Anyanee Kamkaew[3], Kendall E Barrett[3], Eduardo Aluicio-Sarduy[3], Yunan Yang[3], Jonathan W Engle[3], Dawei Jiang[3,4], Weibo Cai[1,3]

[1]Department of Biomedical Engineering, University of Wisconsin-Madison, Madison, WI, USA; [2]Department of Nuclear Medicine, Peking University First Hospital, Beijing, China; [3]Department of Radiology and Medical Physics, University of Wisconsin-Madison, WI, USA; [4]Department of Nuclear Medicine, Union Hospital, Tongji Medical College, Huazhong University of Science and Technology, Wuhan, China. [*]Equal contributors.

Received December 9, 2020; Accepted January 20, 2021; Epub April 15, 2021; Published April 30, 2021

Abstract: With advancement in antibody engineering, the development and characterization of new cancer-specific molecular targets are in the forefront of this PET-antibody combination "revolution". Overexpression of CD146 in different types of tumors, including breast tumor, has been associated with tumor progression and poor prognosis. Non-invasive detection of CD146 with a monoclonal antibody may provide a noninvasive diagnostic tool with high specificity and accountability. Methods: Herein, we have developed a CD146-specific monoclonal antibody (YY146), radiolabeled it with ^{52}Mn and ^{89}Zr and identified its capability in acting as a non-invasive imaging agent that specific targets CD146 in different murine breast cancer models. CD146 expression was first screened in different breast tumor cell lines through Western Blot and confirmed its binding ability to YY146 using Flow Cytometry. Serial immunoPET images were carried out after intravenous administration of ^{52}Mn or ^{89}Zr labeled YY146. In addition, we also performed in vivo fluorescence imaging in animals injected with YY146 conjugated with Cy5.5. Results: Western Blot results show that MDA-MB-435 cell line had greater levels of CD146 expression when compared to the other cell lines investigated. Flow cytometry confirmed binding ability of YY146. PET images revealed well correlated uptake between tumor uptake and CD146 expression levels, confirmed by biodistribution studies and fluorescence imaging. Conclusion: PET imaging, for up to 7 days, of mice bearing three different breast tumors were carried out and revealed radiotracer uptake in tumors that strongly (r^2 = 0.98, P < 0.01), correlated with CD146 expression levels, as confirmed by in vitro and ex vivo studies.

Keywords: ImmunoPET, ^{52}Mn, ^{89}Zr, CD146, YY146, breast cancer, optical imaging

Introduction

In the clinical settings, breast cancer can be distinguished between different subtypes, each with its own prognostic value and management. These subtypes refer to the presence of estrogen receptor (ER) and progesterone receptor (PR) expression, as well as overexpression of HER-2/Neu and those tumors which do not express either are commonly referred to as triple-negative breast cancer (TNBC) [1, 2]. Differential therapeutic regimen is used according to the expression of these three markers. While ER, PR and HER-2/Neu expressing tumors can be treated with specific inhibitors, little options are found for TNBC patients, which end up being treated with unspecific chemotherapeutic agents [3, 4]. Unfortunately, around 10-15% of all breast tumor types are TNBC and patients tend to have a poorer outcome when compared to those with positive markers [5]. In this context, the identification and evaluation of other breast cancer tumor markers are warranted and can have important implications in TNBC diagnosis and therapy. As such, preclinical studies on the identification of novel targets and its in vivo non-invasive detection in the tumor tissue is of upmost importance and can potentially contribute for the development of therapeutic antibodies [6].

Overexpression of CD146, also referred to as melanoma cell adhesion molecule (MCAM, M-CAM and MUC18), have been described for

many types of cancer, including breast cancer [7]. It has been demonstrated that, in breast tumors, CD146 is involved in the induction of epithelial-to-mesenchymal transition (EMT) [8-11], a developmental process [12] frequently involved in cancer dissemination. CD146 has also been associated with poor prognosis and tumor aggressiveness in breast cancer [13-15]. In addition, CD146 correlates with tumors of higher grade, especially on receptor specific negative breast cancer subtypes, such as TNBC [8, 11, 14] and CD146 downregulation is associated with less aggressive phenotypes [14]. With that in mind, CD146 shows promise as a useful marker for predicting disease progression and treatment response in breast cancer patients and could be a potential target for TNBC theranostics.

Herein, we aimed at identifying CD146 expression levels of different breast cancer tumor cell lines, including those derived from TNBC and evaluate the ability of using that target for immunoPET imaging using an anti-CD146 monoclonal antibody (YY146) radiolabeled with ^{52}Mn in orthotopic tumors. In parallel, to dive in the possibilities of applications of YY146 in breast cancer, we have also performed PET imaging on breast cancer xenografts using YY146 radiolabeled with ^{89}Zr and optical imaging with YY146 conjugated with a fluorescent dye.

Methods

Cancer cell lines and animal models

Four human breast cancer cell lines including MDA-MB-231 (HTB26), SKBR-3 (HTB30), MCF-7 (HTB22) and MDA-MB-435 (HTB-129) were used (ATCC; Manassas, VA, USA). Cells were grown in a humidified incubator at 37°C with 5% CO_2 using Dulbecco's Modified Eagle Medium (DMEM) for MDA-MB-231 and MDA-MB-435 cells. Eagle's Minimum Essential Medium (EMEM) for MCF-7 cells and McCoy's 5A Medium for SKBR3 cells with proper supplementation. Cells were used for studies at ~70% confluence.

All animal studies were conducted under the approval of the University of Wisconsin Institutional Animal Care and Use Committee. To generate tumors, cells were resuspended in 100 uL 1:1 of PBS and Matrigel (BD Biosciences) at a concentration of 1×10^6 cells/mL. Orthotopic breast tumor was induced with injection of MDA-MB-231, MDA-MB-435 or MCF-7 cells into the mammary fat pad [16] of four-to-five week old female athymic nude mice (Envigo, WI, USA). Xenograft breast tumor was induced with the injection of MDA-MB-435 or MCF-7 into the right flank of female athymic nude mice (Envigo, WI) and in vivo experiments were carried out approximately 3 weeks after.

Tracer generation (radiolabeling with ^{52}Mn and ^{89}Zr and conjugation with Cy5.5)

^{52}Mn and anti-CD146 production and purification was carried out as previously reported [17, 18]. For radiolabeling of YY146 with ^{52}Mn, YY146 was first conjugated with the chelator p-SCN-Bn-DOTA (DOTA; Macrocyclics, Dallas, TX, USA) according to previously described procedure (pH ~8.5 adjusted with 0.1 M Na_2CO_3, and a YY146:DOTA molar ratio of 1:25, 2 hours at room temperature) [19]. PD-10 columns (GE Healthcare, Aurora, OH, USA) were used to purify DOTA-YY146 from unconjugated DOTA.

For radiolabeling with ^{52}Mn, 150-200-μg of DOTA-YY146, in 0.1 M sodium acetate buffer (pH 4.5) was added to 74-148 MBq (2-4 mCi) of ^{52}Mn (0.1 M HCL) and let react for 30 min at 37°C. ^{52}Mn-DOTA-YY146 was purified using PD-10 with PBS as mobile phase. For radiolabeling with ^{89}Zr, deferoxamine (Df) was first conjugated to YY146 using protocols described previously [20]. YY146-Df radiolabeling was carried out in 0.5 M HEPES buffer, at final pH of 7.0 for 1 h at 37°C with approximately 120 MBq (~3 mCi) of ^{89}Zr-oxalate followed by purification with PD-10 columns.

YY146 or IgG was conjugated with Cy5.5 NHS ester (Abcam) at a molar ratio of 1:20 in a carbonate-bicarbonate buffer (pH 9.2) for 2 h. Cy5.5-YY146 was then purified using PD-10 column with PBS as mobile phase.

Flow cytometry and Western blot

Western blot was carried out to determine presence of CD146 protein, following standard procedure. Mouse anti-CD146 (Santa Cruz Biotech Inc., Dallas, TX) and rabbit anti-β-actin (LI-COR Biosciences) were used as primary antibodies. IRDye-680LT-labeled donkey anti-mouse (1:2000) and IRDye-800CW-labeled

donkey (1:3000) anti-rabbit were used as secondary antibodies (LI-COR Biosciences). Fluorescent immunocomplexes were acquired on Odyssey® CLx Infrared Imaging System (LI-COR Biosciences) and analyzed with Image Studio Lite (LI-COR Biosciences).

Flow cytometry was employed to investigate the CD146-immunoreactivity of YY146 and DOTA-YY146 in different cell lines. For that, cells were were incubated with 5 μg/mL or 25 μg/mL of YY146 and DOTA-YY146 antibodies (30 min, RT). After washing three times, cells were then incubated with FITC-labeled goat anti-mouse IgG (5 μg/mL) for 30 min at RT. Experiment was carried out in a MACSQuant10 cytometer and analyzed in FlowJo software (Tree Star, Inc.).

PET imaging and ex vivo biodistribution studies

1-3 MBq of ^{52}Mn-DOTA-YY146 was intravenously injected in mice bearing MDA-MB-231, MDA-MB-435 and MCF-7 orthotopic tumors. PET scans were acquired (60 million coincidence events) with an Inveon PET/CT scanner (Siemens). Serial PET scans were acquired at 4, 24, 48, 72, 96, 120 and 168 h post-injection (p.i.). Similarly, for imaging with ^{89}Zr-Df-YY146, mice bearing MDA-MB-435 or MCF-7 xenografts were injected with 5-10 MBq ^{89}Zr-Df-YY146 per mouse via tail vein. Imaging was performed at 4, 6, 12, 24, 48 ,72, 96 and 120 h p.i. Images were reconstructed using Inveon Acquisition Workplace (Siemens). regions-of-interest (ROI), expressed as percent injected dose per gram of tissue (%ID/g) were drawn in an Inveon Research Workspace (Siemens). After the last scan, animals were euthanized and major organs were harvested and measured in a gamma counter (PerkinElmer).

In vivo and ex vivo fluorescence imaging

Cy5.5-YY146 was intravenously injected into MDA-MB-435 and MCF-7 xenograft models (n = 3) at a dose of approximately 50 μg per animal. The animals were anesthetized by 2% isoflurane and placed in a prone position on an IVIS Spectrum imager. Fluorescence imaging was collected at 6, 24, 48, 72, 96, 120, 144 and 168 h p.i. using a Living Image 4.0 software, under an excitation wavelength of 675 nm and emission wavelength of 720 nm. The mice were euthanized after the final imaging time point and tumor and major organs including heart, lung, liver, spleen, pancreas, stomach, intestine, kidney, bladder, muscle, bone and brain were harvested for *ex vivo* imaging. As a non-specific control, a separate cohort of animals were injected with Cy5.5-IgG and *in vivo* and *ex vivo* imaging were carried out in the same manner as described above.

Immunofluorescence staining

CD146 expression was further evaluated in excised tumor tissue samples through immunofluorescence staining according to previously described procedure for frozen samples [18, 21, 22]. Samples were also co-stained for CD31, a vasculature marker. YY146 (10 μg/mL) and rat anti-mouse CD31 antibody (BD Biosciences) were used as primary antibodies and AlexaFluor488-labeled goat anti-mouse IgG (Invitrogen) and Cy3-labeled donkey anti-rat IgG (The Jackson Laboratory), as secondaries. Images were acquired with w a Nikon Digital Eclipse C1 plus microscope.

Statistical analysis

GraphPad Prism 5.03 was used for quantitative data analysis. Results are presented as mean ± SD. For statistical analysis, unpaired Student's *t* test, and statistical was used and significance was considered to have *p* values of 0.05 or less. All groups had a minimum of three subjects ($n \geq 3$).

Results

In vitro assays

We first aimed at identifying CD146 expression levels in different breast cancer cell lines, derived from both receptors expressing and TNBC tumors. Data from western blot analysis (**Figure 1A** and **1B**) demonstrate a strong band around 130 kDa, which indicates presence of CD146 protein in at least three out of four cell lines investigated. The expression levels for the cells tested were MDA-MB-435 > MDA-MB-231 > SKBR3 > MCF-7 (MDA-MB-435 presented highest expression and MCF-7 lowest expression). In order to evaluate if our tracer could differentiate and accumulate differently in tumor tissue according to CD146 expression, we have selected MDA-MB-435 cell line as our high-expression cell line, MDA-MB-

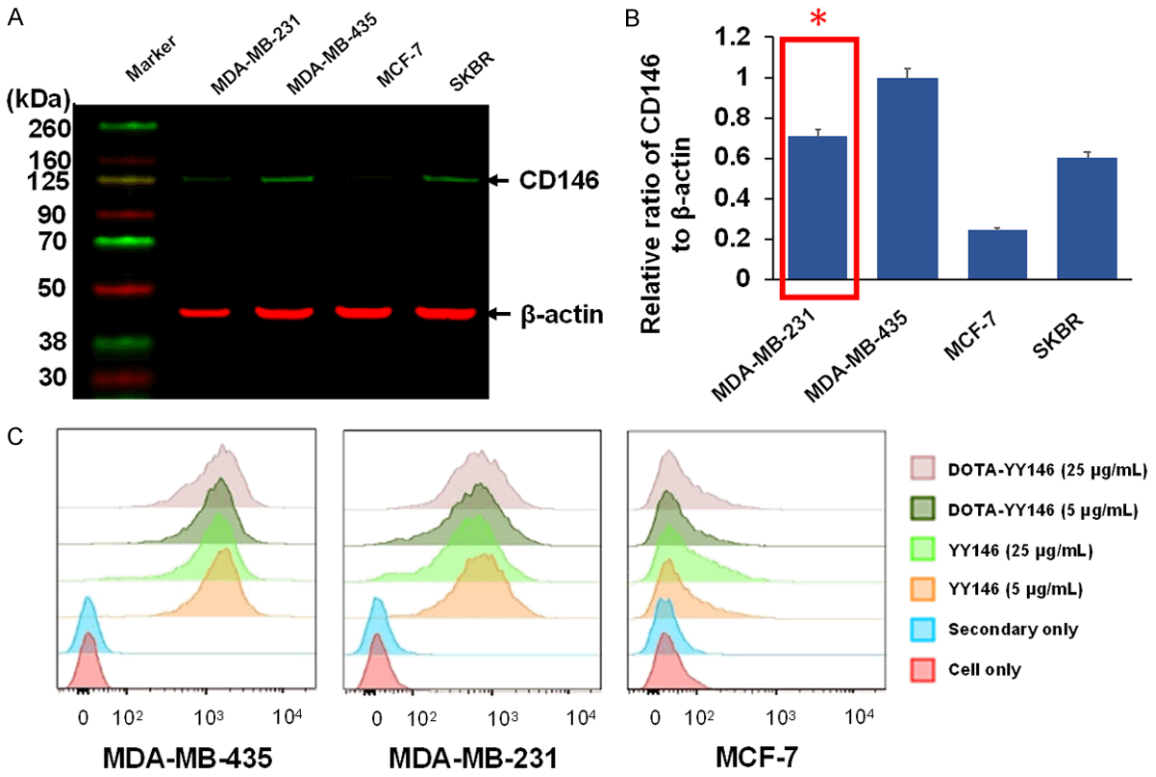

Figure 1. *In vitro* CD146 expression in human breast cancer cells. A. Western blot displayed bands around 130 kDa consistent with CD146 (113 kDa). B. Quantification of Western blot findings. Expression levels of CD146 for different cell lines followed the order MDA-MB-435 > MDA-MB-231 > SKBR-3 > MCF-7. *Red rectangle identifies TNBC cell line. C. Fluorescence histogram from Flow cytometry of different cell lines and immunoreactivity of YY146 bound and unbound to chelator.

231 as our medium expression level cell line and MCF-7 as our low CD146 expression cell line for future *in vivo* studies. Noteworthy, we selected two TNBC-derived cancer cell lines (MDA-MB-435 and MDA-MB-231). We also confirmed this trend through flow cytometry (**Figure 1C**), in which histograms showed fluorescence signals corresponding to CD146 expression levels similarly as found for Western Blot. Importantly, flow cytometry confirmed that CD146-avidity of YY146 was not affected by the presence of DOTA chelator. Of note, we have previously reported that the conjugation of YY146 with Df did not affect its binding ability [20].

Radiolabeling studies

To establish a radiolabeling protocol, we first evaluated the time of incubation and optimal amount of antibody per mCi of activity that would allow good radiolabeling yields. Results of radiolabeling study are presented in Figure S1, in which different amounts of antibody per mCi of isotope were tested and labeling yields were calculated as a function of incubation time using iTLC. Rapid and high-yield labeling was observed for all the concentrations tested that reached above 95% labeling yield after 60 min incubation. We then selected 250 μg/mCi to be used in our standard procedures. Of note, herein we found similar results to findings from our group in previously published reports of YY146 labeling studies with ^{89}Zr [20, 21].

PET imaging and biodistribution studies

After intravenous administration of ^{52}Mn-DOTA-YY146 in mice bearing MDA-MB-435, MDA-MB-231 or MCF-7 orthotopic tumors, serial PET images were acquired at different time points for up to 7 days (**Figure 2A**). In accordance to *in vitro* findings, PET imaging revealed that tumors in MDA-MB-435 and MDA-MB-231 tumor-bearing mice were clearly visualized since 24 h p.i. onward. However, MDA-MB-435

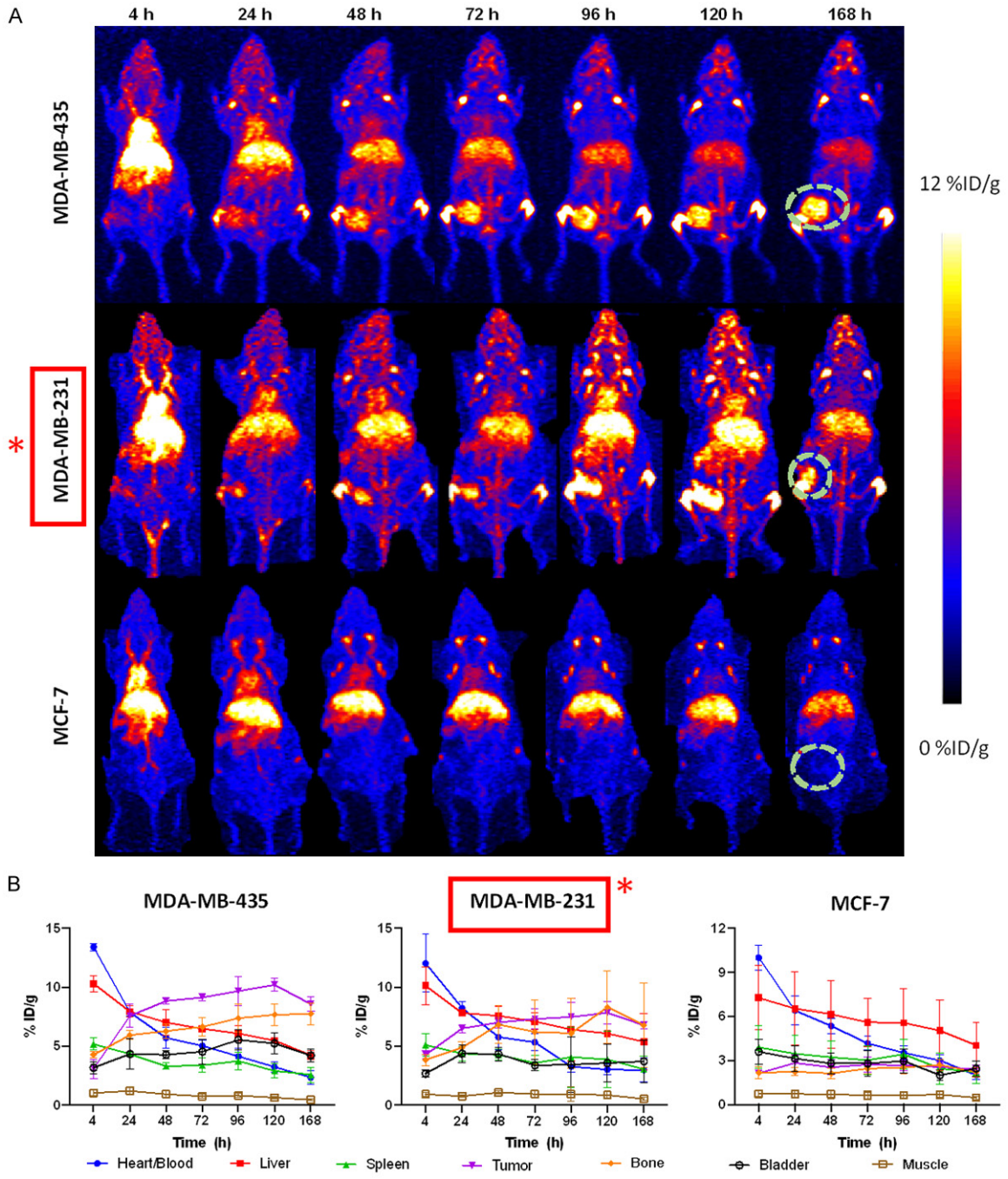

Figure 2. PET imaging results. A. Serial maximum intensity projection (MIP) PET Images at different time points after injection of ^{52}Mn-DOTA-YY146 in mice bearing MDA-MB-435, MDA-MB-231, or MCF-7 tumors. Green dashed circles refer to the location of orthotopic tumors. *Red rectangle identifies TNBC cell line. B. Time Activity Curves calculated from PET imaging ROI analysis of the aforementioned groups.

tumor bearing mice had the highest tumor accumulation among the other tested groups, tumor uptake increased over time and reach a maximum of 10.2 ± 0.5 %ID/g at 120 h p.i. (**Figure 2B**). For the MDA-MB-231 tumor bearing mice group, the tumor reached its highest at 120 h p.i., 7.8 ± 0.9 %ID/g with significantly lower uptake when compared to MDA-MB-435 group starting from 48 h p.i. time point (**Figure 3A**). MCF-7 tumor bearing mice had near background tumor uptake *in vivo*, with its highest at 2.8 ± 0.6 %ID/g at 24 h p.i. MCF-7 group had

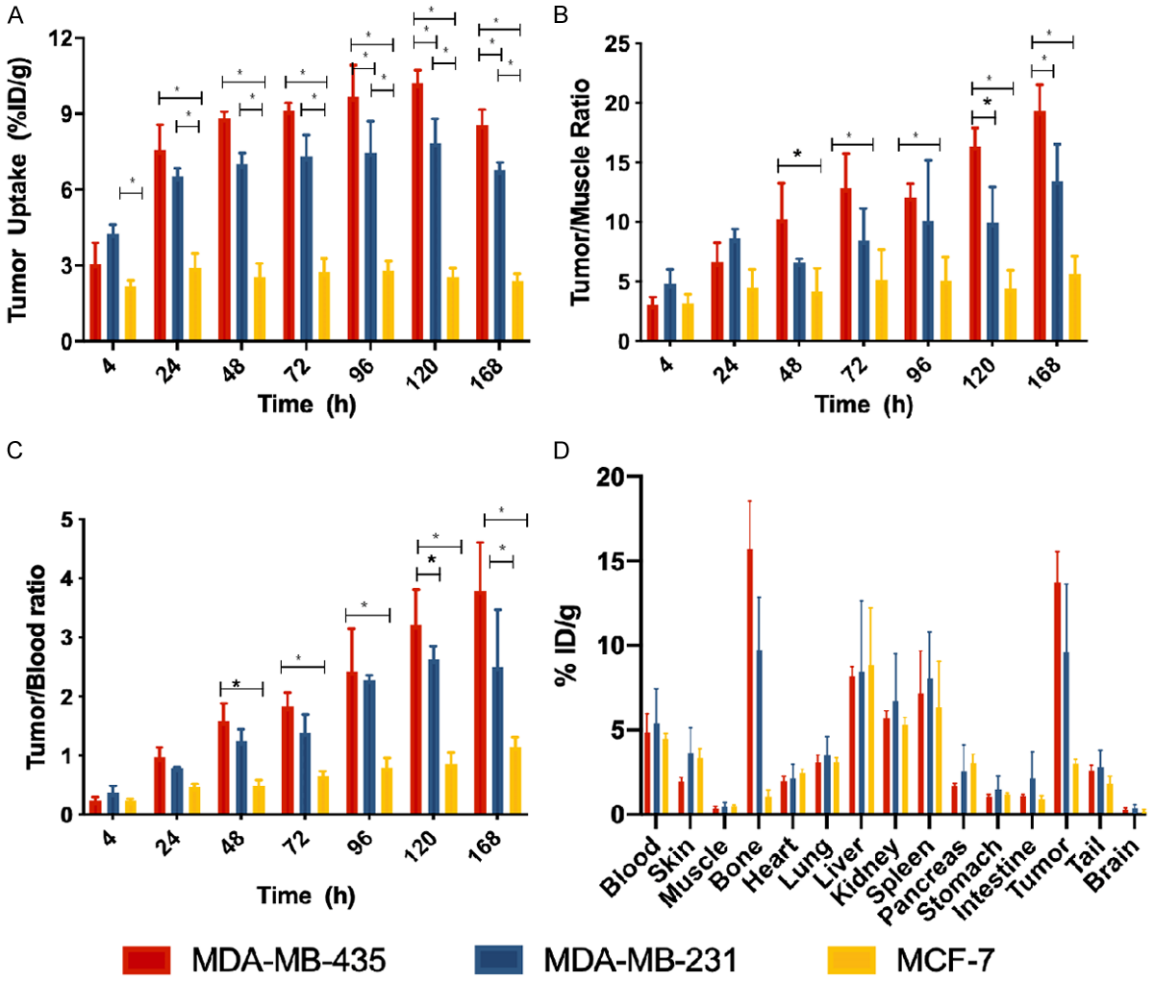

Figure 3. PET ROI analysis and biodistribution data. Direct comparison of (A) Tumor uptake, (B) Tumor-to-muscle, and (C) Tumor-to-blood ratios based on the quantitative data obtained from the analysis of PET images. *P < 0.05. (D) Ex vivo gamma counting biodistribution at 168 h post-injection of ^{52}Mn-DOTA-YY146 in mice bearing MDA-MB-435, MDA-MB-231 or MCF-7 tumors.

significantly lower tumor uptake when compared to the other two groups since 24 h p.i. onward. A direct comparison between tumor uptake can be seen at **Figures 4B**, **5**. Tumor uptake in MDA-MB-435 tumor bearing mice was significantly higher than that of MCF-7 tumor group since 24 h p.i. and significantly higher than MDA-MB-231 group starting at 48 h p.i. In addition, direct comparisons of tumor-to-muscle (**Figure 3B**) and tumor-to-blood (**Figure 3C**) ratios were calculated. In both cases, the ratios for MDA-MB-435 implanted group is significantly higher than MCF-7 group starting from day 2 p.i. and MDA-MB-231 implanted mice from 120 h p.i. Of note, tumor-to-blood ratios reached its highest value of 3.8 ± 0.8 %ID/g at 168 h p.i., 2.6 ± 0.2 at 129 h %ID/g p.i. and 1.1 ± 0.2 %ID/g at 168 h p.i. in MDA-MB-435, MDA-MB-231 and MCF-7 tumors respectively. More importantly, tumor-to-muscle ratios reached unprecedented high values in the triple-negative breast cancer cell lines, with values of 19.3 ± 2.2 and 13.4 ± 3.1 %ID/g for MDA-MB-435 and MDA-MB-231, respectively.

Altogether, those results demonstrated the ability of ^{52}Mn-DOTA-YY146 in differentiating CD146 expression levels *in vivo*. The tracer cleared from the circulation in a similar manner in all groups investigated. Liver was found to be the off-target organ with the highest uptake among all groups, with uptakes that peaked at 4 h p.i. at 10.3 ± 0.7 %ID/g, 10.1 ±

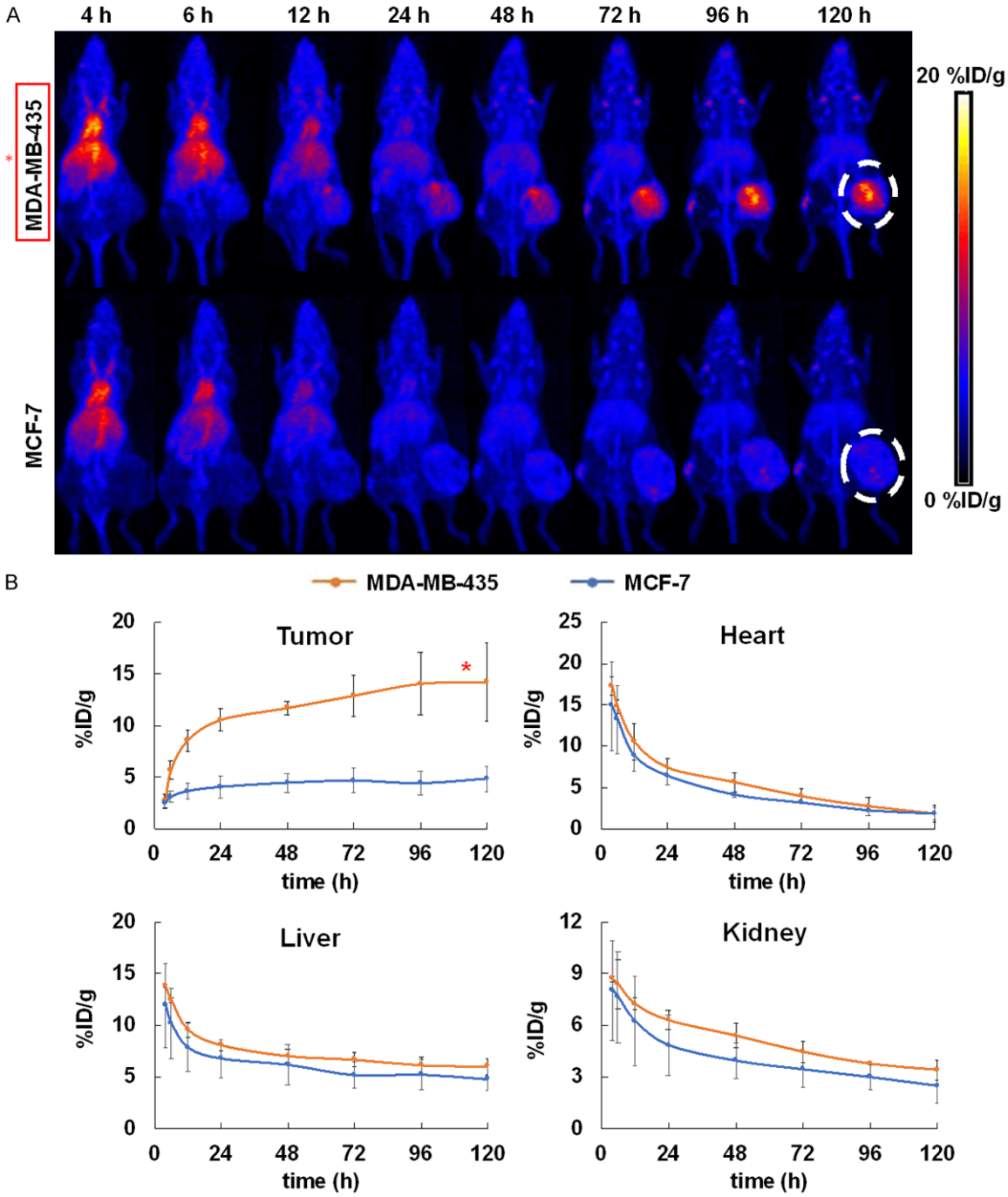

Figure 4. ^{89}Zr-Df-YY146 PET imaging and ROI analysis of PET images in MDA-MB-435 and MCF-7 subcutaneous xenograft models. A. MIP PET images indicating that the tumor radioactivity uptake of MDA-MB-435 gradually increased, while the MCF-7 tumor was close to the background. The white circle depicts tumor area. *Red rectangle identifies TNBC cell line. B. ROI analysis of PET images showed tumor peak uptake of ^{89}Zr-Df-YY146 in MDA-MB-435 was 14.05 ± 3.04 %ID/g at 120 h p.i., while in the MCF-7 model was only 4.65 ± 1.20 %ID/g (n = 4, $P < 0.05$). The radioactive uptake of the blood, liver and kidney showed a gradual decrease trend ($P > 0.05$).

1.6 %ID/g and 7.3 ± 2.2 %ID/g for MDA-MB-435, MDA-MB-231 and MCF-7 groups respectively, which corresponds to the antibody-based tracer clearance kinetics. Relatively important signal in bone tissue was observed in all the studied groups, which usually indicates

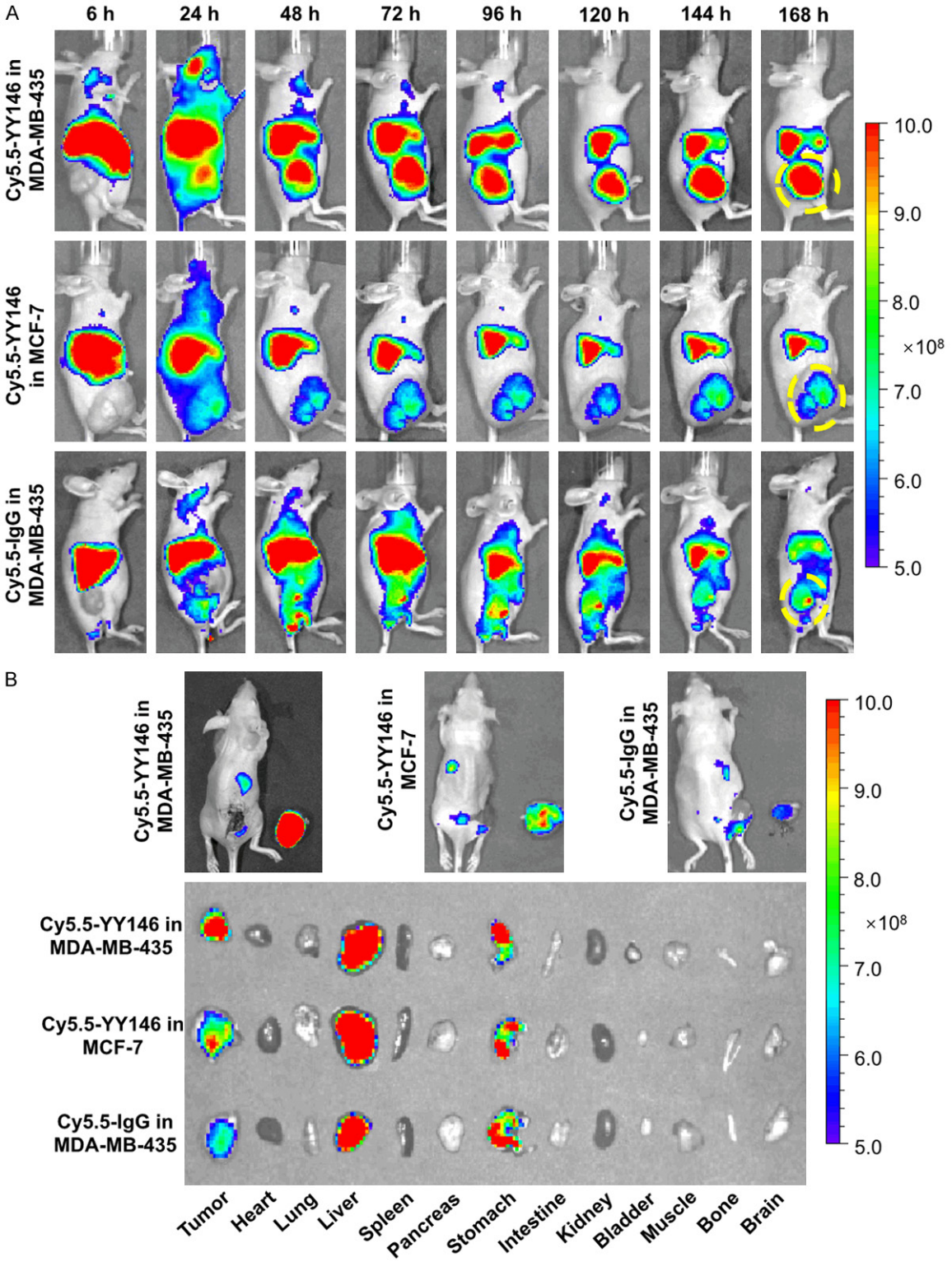

Figure 5. Near infra-red fluorescence imaging results. A. Serial in vivo fluorescence of MB-435 and MCF-7 tumor bearing animals injected with YY146-Cy5.5 or IgG-Cy5.5. Tumors are indicated by yellow circles. B. *Ex vivo* imaging of animals after tumors were harvested as well as main organs confirmed the results of *in vivo* imaging.

certain metal-chelate instability. However, free manganese has been shown to have a different pharmacokinetic profile and typically do not accumulate in the bones [23]. Herein, a

direct interaction between the bone and DOTA-bound manganese might account for this bone accumulation, but further studies are warranted. Nonetheless, the use of ^{52}Mn is still warranted for longer-term scanning, or its use in novel triple coincidence PET cameras. We also observed some uptake in lymph nodes, which could be explained by the fact that CD146 is also expressed on endothelial cells, such as the high endothelial venules in lymph nodes [24]. *Ex vivo* biodistribution studies confirmed *in vitro* and *in vivo* PET findings (Figure S2), and tumor uptake followed the MDA-MB-435 > MDA-MB-231 > MCF-7 trend at 13.7 ± 1.8 %ID/g, 9.6 ± 4.0 %ID/g and 3.0 ± 0.3 %ID/g respectively.

Inspired by the previous results and the fact that the ^{52}Mn is still a relatively novel PET isotope, we have decided to investigate differential tumor uptake of YY146 by radiolabeling it with a different and more commonly used isotope, ^{89}Zr. Since ^{89}Zr has a half-life (78.4 h) that allows PET imaging of similar time points as ^{52}Mn, we were able to make a direct comparison between ^{52}Mn and ^{89}Zr labeled YY146. In those studies, we selected the cell lines with highest and lowest CD146 expression and tumor uptake in previous studies, MDA-MB-435 and MCF-7, respectively. The maximum intensity projection (MIP) images of animals injected with ^{89}Zr-Df-YY146 showed similar pattern as that observed from the animals injected with ^{52}Mn-DOTA-YY146, in which tumor uptake is clearly visualized in MDA-MB-435 tumor-bearing mice after 24 h p.i. (**Figure 4A**). Tumor uptake in MDA-MB-435 tumor bearing mice increased gradually with time and peaked at 14.2 ± 3.8 %ID/g (n = 3) at 120 h p.i., while MCF-7 tumor uptake was close to background at all time points, with a maximum uptake of 4.85 ± 1.20 %ID/g also at 120 h p.i. (**Figure 4B**). Uptake in MDA-MB-435 tumors were significantly higher ($P < 0.05$) than uptake in MCF-7 tumors starting from 12 h p.i. until the end of the study. Furthermore, uptake in non-target organs such as heart, liver, and kidney (**Figure 4B**) gradually decreased over time, and there was no statistical difference between the two groups ($P > 0.05$).

Of note, biodistribution of ^{52}Mn-DOTA-YY146 was very similar to that of ^{89}Zr-Df-YY146, and no uptake differences in the blood pool, liver and bone was found between the groups at all time points investigated, except that of liver at 4 h p.i. (Figure S3). More importantly, tumor uptake in MDA-MB-435 tumor bearing mice was also not different between the two injected probes (Figure S4A). However, in MCF-7 tumors, even though the uptake was significantly lower than that of MDA-MB-435 tumors in both groups, the group injected with ^{89}Zr-Df-YY146 had significantly higher tumor uptake from 48 h p.i. onward than the group injected with ^{52}Mn-DOTA-YY146 (Figure S4B), probably due to differences in EPR effect of subcutaneous vs orthotopic xenografts.

Fluorescence imaging

In vivo fluorescence imaging was performed at 6, 24, 48, 72, 96, 120, 144 and 168 hours after administration of YY146 conjugated with Cy5.5 (**Figure 5A**). A separate cohort of MDA-MB-435 tumor bearing animals were injected with IgG-Cy5.5 as a control group. Results were compatible with findings from PET images, in which tumor uptake gradually increased over time and tumor uptake in MDA-MB-435 tumor bearing mice was significantly higher than that found for MCF-7 tumor bearing mice (Figure S5). In addition, uptake in MDA-MB-435 tumors were significantly higher than tumor uptake in animals injected with IgG-Cy5.5. Of note, tumor uptake of MDA-MB-435 tumors in animals injected with IgG-Cy5.5 was similar to that found for MCF-7 tumors injected with YY146-Cy5.5, mostly due to EPR effect. Also corroborate by findings from PET, uptake in the liver fluorescence decreased with time, and there was no significant difference among the groups. At the last time point of imaging (168 h p.i.), mice were euthanized and tumors and main organs were harvested for *ex vivo* fluorescence imaging (**Figure 5B**). The tumor fluorescence uptake level was consistent with *in vivo* imaging. Fluorescence mainly remained in the liver and stomach, indicating that the antibody may be excreted mainly through the liver and digestive system (Figure S5).

Immunofluorescence staining

Immunofluorescence staining of tumor sections confirmed *in vitro* studies findings and were in accordance with findings from PET (**Figure 6**). Tissue sections of different tumors were co-stained for CD146 and CD31 (vascula-

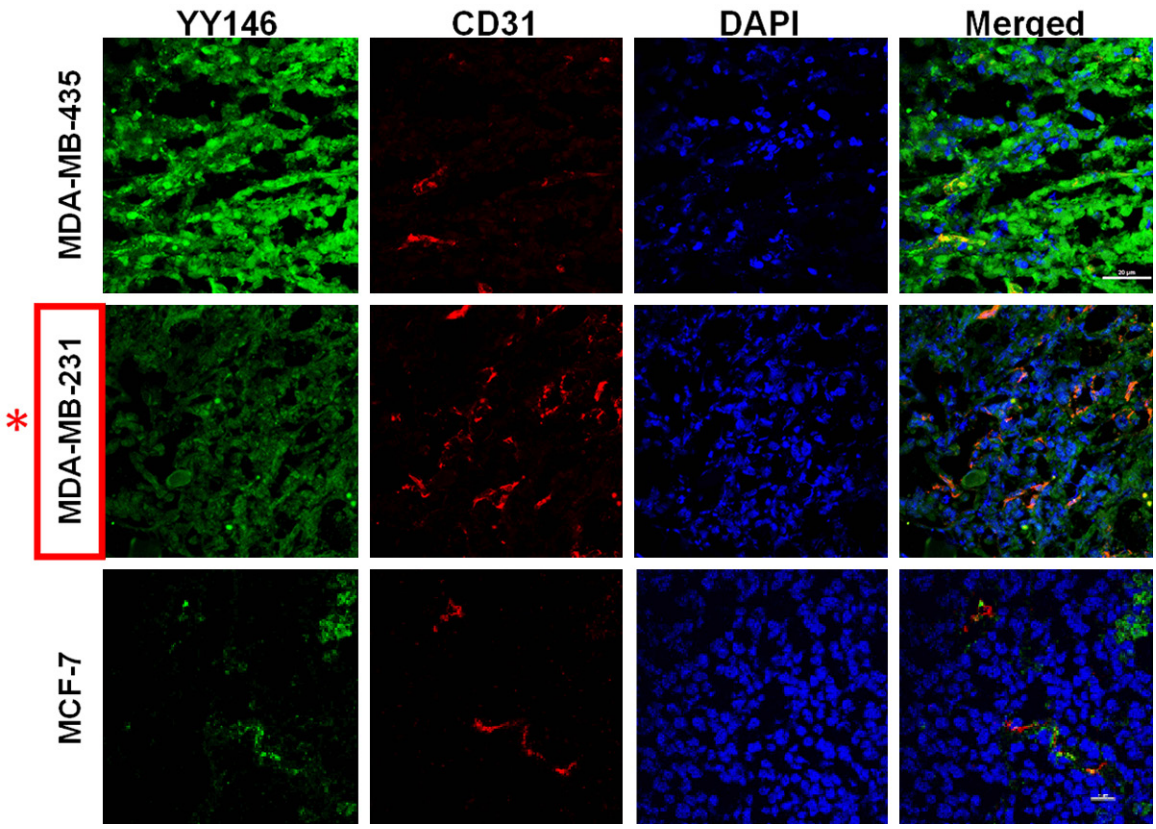

Figure 6. Immunofluorescence staining data. CD146/CD31 immunofluorescence staining of different human breast cancer tumors. CD146 staining (green channel) was more prominent in MDA-MB-435 tumors. The overlap between CD146 and CD31 (red channel) can also be seen. Scale bar: 20 μm. *Red rectangle identifies TNBC cell line.

ture). In animals implanted with MDA-MB-435 cells, very high CD146 signal is seen over the entire sample, while MDA-MB-231 and MCF-7 tissue sections showed medium and minimal staining of CD146, respectively. CD31 staining identifies similar vasculature among samples.

Discussion

Approximately 1 in 8 women (around 12%) in the United States will be diagnosed with an invasive form of breast cancer over the course of her lifetime. Last year alone, more than 320,000 new cases of breast cancer were expected to be diagnosed in the U.S., of which more than 80% with an invasive form of the disease [25]. Worldwide, the estimated incidence of breast cancer per year is more than 2 million new cases making breast cancer the second most incident tumor among women. Among those cases, more than 200,000 (10-15%) new cases annually will be of triple negative breast cancer, characterized by aggressive behavior, metastatic spread and poor survival rates. Those characteristics are due primarily to the fact that, at the time of diagnosis, tumors are already larger with positive axillary lymph node and poorer Nottingham prognostic index [26]. In addition, TNBC is intrinsically heterogeneous in its molecular, immunological and clinical behavior, contributing to different clinical outcomes. After years without breakthroughs in TNBC treatment or diagnosis, the scientific community has undertaken a great effort in understanding the different molecular profiles and to discover new molecular targets for TNBC [27-29]. Recent advances have been made with the inclusion of PARP inhibitors and checkpoint inhibitors, and other potential predictive and prognostic biomarkers have been found [26, 30]. However, cytotoxic chemotherapy is still the primary therapeutic agent against TNBC and a comprehensive classification of TNBC with specific molecular phenotypes has yet to be defined. In this context, identifying practical immune-molecular TNBC

signatures would be highly desirable for accurate targeted diagnosis, patient stratification, personalized therapy and overall disease management [31].

In breast cancer, CD146 overexpression is associated with poor prognosis, hormonal treatment resistance and with a tumor of higher grade. Most recently, it has been shown that CD146 is found in around 11% of all primary breast cancer tissues and its predominantly present in the medullary and triple-negative subtypes [32]. Our group has previously developed an anti-human CD146-targeting monoclonal antibody, YY146, and successfully demonstrated its ability, *in vivo,* of targeting CD146 in a variety of tumor models [18, 19, 21]. In this study, we aimed at validating CD146 as a target for noninvasive diagnosis and stratification of TNBC and to evaluate its potential as a therapeutic target. To the best of our knowledge, this is the first time a CD146 target immunoPET probe is used for *in vivo* diagnosis and stratification of TNBC.

Herein, small animal ImmunoPET imaging followed by *ex vivo* biodistribution studies were carried out in orthotopic breast tumors, including of cell lines derived from TNBC. After delineating CD146 expression of different cell lines, *in vivo* tumor accumulation of the tracer according to CD146 expression levels was investigated in different breast cancer cell lines (MDA-MB-435, MDA-MB-231 and MCF-7), including at least one of TNBC. In accordance with *in vitro* data, PET imaging demonstrated a good correlation between CD146 expression levels and tumor uptake, in which the TNBC cell lines had higher expression levels and tracer tumor accumulation than that of MCF-7 cell line. Furthermore, the different levels of expression among the CD146 expressing cell lines was clearly delineated through PET imaging and resulted in excellent differential tumor-to-muscle ratios of 19.3 ± 2.2 for MDA-MB-435 tumor bearing mice and 13.4 ± 3.1 for animals with MDA-MB-231 tumors. Tracer uptake in MCF-7 tumors only reached a tumor-to-muscle ratio of 5.6 ± 1.5, confirming further the correlation between ^{52}Mn-DOTA-YY146 uptake and CD146 expression.

Nuclear medicine has been facing great need for long-lived PET radiometals due to the advancement of antibody-based cancer therapeutics and the need for companion diagnostics [33, 34]. ^{52}Mn is a radioisotope with interesting decay characteristics ($t_{1/2}$ = 5.59 d, β^+ = 29.6%, $E_{\beta ave}$ = 0.24 MeV) and have been increasingly used in the recent years because of its use in PET/MRI techniques. When compared to other commonly used isotopes, such as ^{64}Cu or ^{89}Zr, ^{52}Mn can offer advantages in immunoPET-based studies in which longer study time-points (up to 3 weeks) are needed. Furthermore, when used as a companion diagnostic tool, for example together with the use of long-lived nuclides such as ^{177}Lu, the entire course of treatment can be evaluated with ^{52}Mn PET [23]. In addition, because of its high amount of coincident high energy gammas, ^{52}Mn is uniquely suited for third-gamma coincidence PET [35]. Our group have previously demonstrated the production, purification and labeling procedures of ^{52}Mn and its application in immunoPET imaging [23]. Herein, we also demonstrate the ability in using ^{52}Mn as a PET isotope with an appropriate half-life that matches antibody pharmacokinetics *in vivo,* with the animals being monitored for up to 7 days. Most importantly, since the tumor uptake peaked at 120 h p.i., it was critical to use an isotope with a larger half-life than the most commonly used ^{64}Cu or ^{68}Ga. Notably, we found no significantly different pharmacokinetics between ^{52}Mn-DOTA-YY146 and ^{89}Zr-Df-YY146 as demonstrated by PET images and ROI calculations.

To demonstrate even further the application possibilities of YY146, we conjugated it with a near-infrared fluorescence-emitting dye to allow for optical imaging. When compared to other imaging techniques, optical imaging can have several advantages including versatility, sensitivity, great spatial resolution and has become a widely used tool in all pre-clinical studies [36]. Fluorescence imaging corroborated findings from PET and differential CD146 expression directly correlated with tracer uptake. Even though neoadjuvant therapy is the gold standard for TNBC treatment, surgical treatment with breast preservation has been proposed [37]. In this context, real-time near infra-red Fluorescence (NIRF) imaging with a target specific probe such as YY146-Cy5.5 can be complimentary to PET imaging findings in the clinical setting and used for surgical margins identification and tumor resection assess-

ment. We have also performed imaging with IgG and results indicated tracer specificity and tumor uptake in high CD146 expressing cell line was similar to that of low expressing one. Specificity, *in situ* CD146 expression and its differential tumor uptake was further demonstrated by *ex vivo* immunofluorescence staining of tumor tissue. Taken together, our data reveal the ability of our radiolabeled probe in identifying different CD146 expression levels *in vivo* and its potential as an imaging agent targeting TNBC. This can have important implications in TNBC management such as diagnosis, stratification, staging and identification of patients who will most likely respond to CD146-targeted therapies.

Conclusion

We have evaluated and characterized the ability of ^{52}Mn-labeled YY146, a specific antibody targeting human CD146 to act as a CD146-specific breast tumor imaging agent, with capability of delineating different CD146 expressions. PET imaging, for up to 7 days, of mice bearing three different breast tumors were carried out and revealed radiotracer uptake in tumors that strongly ($r^2 = 0.98$, $P < 0.01$) correlated with CD146 expression levels, as confirmed by *in vitro* and *ex vivo* studies. Herein, we confirmed the ability of using YY146 as *in vivo* targeting agent for non-invasive imaging (PET and NIRF) in breast cancer models. Since overexpression of CD146 has been identified in a diverse range of tumors and most specifically triple negative breast cancer, we expect this radiolabeled antibody to hold a significant role in TNBC diagnosis, patient stratification and treatment response monitoring.

Acknowledgements

This work was supported, in part, by the University of Wisconsin-Madison, the National Institutes of Health (P30CA014520 and T32-CA009206), the Brazilian Science without Borders Program (SwB-CNPq), the National Natural Science Foundation of China (8187-1385), PKU medicine-X Youth Program (PKU-2020LCXQ007 and PKU2021LCXQ023) and Open Funding Project of the State Key Laboratory of Biochemical Engineering (2020KF-01).

Disclosure of conflict of interest

None.

Address correspondence to: Weibo Cai, Department of Biomedical Engineering, University of Wisconsin-Madison, Room 7137, 1111 Highland Ave, Madison, WI 53705-2275, USA. Tel: 608-262-1749; Fax: 608-265-0614; E-mail: wcai@uwhealth.org; Lei Kang, Department of Nuclear Medicine, Peking University First Hospital, No. 8 Xishiku Street, Xicheng District, Beijing 100034, China. Tel: +86-10-8357-5252; Fax: +86-10-8357-2914; E-mail: kanglei@bjmu.edu.cn; Dawei Jiang, Department of Nuclear Medicine, Union Hospital, Tongji Medical College, Huazhong University of Science and Technology, Wuhan, China. E-mail: daweijiang@hust.edu.cn

References

[1] Brenton JD, Carey LA, Ahmed AA and Caldas C. Molecular classification and molecular forecasting of breast cancer: ready for clinical application? J Clin Oncol 2005; 23: 7350-7360.

[2] Velikyan I, Schweighöfer P, Feldwisch J, Seemann J, Frejd FY, Lindman H and Sörensen J. Diagnostic HER2-binding radiopharmaceutical, [(68)Ga]Ga-ABY-025, for routine clinical use in breast cancer patients. Am J Nucl Med Mol Imaging 2019; 9: 12-23.

[3] Chavez KJ, Garimella SV and Lipkowitz S. Triple negative breast cancer cell lines: one tool in the search for better treatment of triple negative breast cancer. Breast Dis 2010; 32: 35-48.

[4] Wang CY, Chiao CC, Phan NN, Li CY, Sun ZD, Jiang JZ, Hung JH, Chen YL, Yen MC, Weng TY, Chen WC, Hsu HP and Lai MD. Gene signatures and potential therapeutic targets of amino acid metabolism in estrogen receptor-positive breast cancer. Am J Cancer Res 2020; 10: 95-113.

[5] Anders CK and Carey LA. Biology, metastatic patterns, and treatment of patients with triple-negative breast cancer. Clin Breast Cancer 2009; 9 Suppl 2: S73-S81.

[6] Scott AM, Allison JP and Wolchok JD. Monoclonal antibodies in cancer therapy. Cancer Immun 2012; 12: 14.

[7] Lehmann JM, Riethmuller G and Johnson JP. MUC18, a marker of tumor progression in human melanoma, shows sequence similarity to the neural cell adhesion molecules of the immunoglobulin superfamily. Proc Natl Acad Sci U S A 1989; 86: 9891-9895.

[8] Zeng Q, Li W, Lu D, Wu Z, Duan H, Luo Y, Feng J, Yang D, Fu L and Yan X. CD146, an epithelial-

mesenchymal transition inducer, is associated with triple-negative breast cancer. Proc Natl Acad Sci U S A 2012; 109: 1127-1132.
[9] Zeng Q, Zhang P, Wu Z, Xue P, Lu D, Ye Z, Zhang X, Huang Z, Feng J, Song L, Yang D, Jiang T and Yan X. Quantitative proteomics reveals ER-alpha involvement in CD146-induced epithelial-mesenchymal transition in breast cancer cells. J Proteomics 2014; 103: 153-169.
[10] Imbert AM, Belaaloui G, Bardin F, Tonnelle C, Lopez M and Chabannon C. CD99 expressed on human mobilized peripheral blood CD34+ cells is involved in transendothelial migration. Blood 2006; 108: 2578-2586.
[11] Jang MH, Kim HJ, Kim EJ, Chung YR and Park SY. Expression of epithelial-mesenchymal transition-related markers in triple-negative breast cancer: ZEB1 as a potential biomarker for poor clinical outcome. Hum Pathol 2015; 46: 1267-1274.
[12] Micalizzi DS and Ford HL. Epithelial-mesenchymal transition in development and cancer. Future Oncol 2009; 5: 1129-1143.
[13] Zabouo E, Imbert AM, Moreau T, Jacquemier J, Birnbam D and Chabannon C. CD146 and breast cancer migration. Cancer Res 2007; 67: 5711.
[14] Zabouo G, Imbert AM, Jacquemier J, Finetti P, Moreau T, Esterni B, Birnbaum D, Bertucci F and Chabannon C. CD146 expression is associated with a poor prognosis in human breast tumors and with enhanced motility in breast cancer cell lines. Breast Cancer Res 2009; 11: R1.
[15] Garcia S, Dales JP, Charafe-Jauffret E, Carpentier-Meunier S, Andrac-Meyer L, Jacquemier J, Andonian C, Lavaut MN, Allasia C, Bonnier P and Charpin C. Poor prognosis in breast carcinomas correlates with increased expression of targetable CD146 and c-Met and with proteomic basal-like phenotype. Hum Pathol 2007; 38: 830-841.
[16] Zhang GL, Zhang Y, Cao KX and Wang XM. Orthotopic injection of breast cancer cells into the mice mammary fat pad. J Vis Exp 2019.
[17] Barrett KE, Aluicio-Sarduy E, Olson AP, Kutyreff CJ, Ellison PA, Barnhart TE, Nickles RJ and Engle JW. Radiochemical isolation method for the production of (52g)Mn from (nat)Cr for accelerator targets. Appl Radiat Isot 2019; 146: 99-103.
[18] Yang Y, Hernandez R, Rao J, Yin L, Qu Y, Wu J, England CG, Graves SA, Lewis CM and Wang P. Targeting CD146 with a 64 Cu-labeled antibody enables in vivo immunoPET imaging of high-grade gliomas. Proc Natl Acad Sci U S A 2015; 112: E6525.
[19] England CG, Jiang D, Hernandez R, Sun H, Valdovinos HF, Ehlerding EB, Engle JW, Yang Y, Huang P and Cai W. ImmunoPET imaging of CD146 in murine models of intrapulmonary metastasis of non-small cell lung cancer. Mol Pharm 2017; 14: 3239-3247.
[20] Hernandez R, Sun H, England CG, Valdovinos HF, Ehlerding EB, Barnhart TE, Yang Y and Cai W. CD146-targeted immunoPET and NIRF imaging of hepatocellular carcinoma with a dual-labeled monoclonal antibody. Theranostics 2016; 6: 1918-1933.
[21] Hernandez R, Sun H, England CG, Valdovinos HF, Barnhart TE, Yang Y and Cai W. ImmunoPET imaging of CD146 expression in malignant brain tumors. Mol Pharm 2016; 13: 2563-2570.
[22] Yang Y, Zhang Y, Hong H, Liu G, Leigh BR and Cai W. In vivo near-infrared fluorescence imaging of CD105 expression during tumor angiogenesis. Eur J Nucl Med Mol Imaging 2011; 38: 2066-2076.
[23] Graves SA, Hernandez R, Fonslet J, England CG, Valdovinos HF, Ellison PA, Barnhart TE, Elema DR, Theuer CP, Cai W, Nickles RJ and Severin GW. Novel preparation methods of (52)Mn for immunoPET imaging. Bioconjug Chem 2015; 26: 2118-2124.
[24] Schrage A, Loddenkemper C, Erben U, Lauer U, Hausdorf G, Jungblut PR, Johnson J, Knolle PA, Zeitz M, Hamann A and Klugewitz K. Murine CD146 is widely expressed on endothelial cells and is recognized by the monoclonal antibody ME-9F1. Histochem Cell Biol 2008; 129: 441-451.
[25] Momenimovahed Z and Salehiniya H. Epidemiological characteristics of and risk factors for breast cancer in the world. Breast Cancer (Dove Med Press) 2019; 11: 151-164.
[26] da Silva JL, Cardoso Nunes NC, Izetti P, de Mesquita GG and de Melo AC. Triple negative breast cancer: a thorough review of biomarkers. Crit Rev Oncol Hematol 2020; 145: 102855.
[27] Gelezhe PB, Blokhin IA, Marapov DI and Morozov SP. Quantitative parameters of MRI and (18)F-FDG PET/CT in the prediction of breast cancer prognosis and molecular type: an original study. Am J Nucl Med Mol Imaging 2020; 10: 279-292.
[28] Cheuk IW, Siu MT, Ho JC, Chen J, Shin VY and Kwong A. ITGAV targeting as a therapeutic approach for treatment of metastatic breast cancer. Am J Cancer Res 2020; 10: 211-223.
[29] Sun X, Ma J, Chen Q, Hou Z, Luo X, Wang G, Wang J, Hu J and Cao Z. SIX4 promotes metastasis through STAT3 activation in breast cancer. Am J Cancer Res 2020; 10: 224-236.
[30] Bianchini G, Balko JM, Mayer IA, Sanders ME and Gianni L. Triple-negative breast cancer: challenges and opportunities of a heteroge-

neous disease. Nat Rev Clin Oncol 2016; 13: 674-690.
[31] Mehanna J, Haddad FG, Eid R, Lambertini M and Kourie HR. Triple-negative breast cancer: current perspective on the evolving therapeutic landscape. Int J Womens Health 2019; 11: 431-437.
[32] de Kruijff IE, Timmermans AM, den Bakker MA, Trapman-Jansen AMAC, Foekens R, Meijer-Van Gelder ME, Oomen-de Hoop E, Smid M, Hollestelle A, van Deurzen CHM, Foekens JA, Martens JWM and Sleijfer S. The prevalence of CD146 expression in breast cancer subtypes and its relation to outcome. Cancers (Basel) 2018; 10: 134.
[33] Deri MA, Zeglis BM, Francesconi LC and Lewis JS. PET imaging with (8)(9)Zr: from radiochemistry to the clinic. Nucl Med Biol 2013; 40: 3-14.
[34] Dash A and Chakravarty R. Radionuclide generators: the prospect of availing PET radiotracers to meet current clinical needs and future research demands. Am J Nucl Med Mol Imaging 2019; 9: 30-66.
[35] Lang C, Habs D, Parodi K and Thirolf PG. Submillimeter nuclear medical imaging with high sensitivity in positron emission tomography using β+γ coincidences. J Instrum 2014; 9: P01008.
[36] Leblond F, Davis SC, Valdes PA and Pogue BW. Pre-clinical whole-body fluorescence imaging: review of instruments, methods and applications. J Photochem Photobiol B 2010; 98: 77-94.
[37] Medina MA, Oza G, Sharma A, Arriaga LG, Hernandez Hernandez JM, Rotello VM and Ramirez JT. Triple-negative breast cancer: a review of conventional and advanced therapeutic strategies. Int J Environ Res Public Health 2020; 17: 2078.

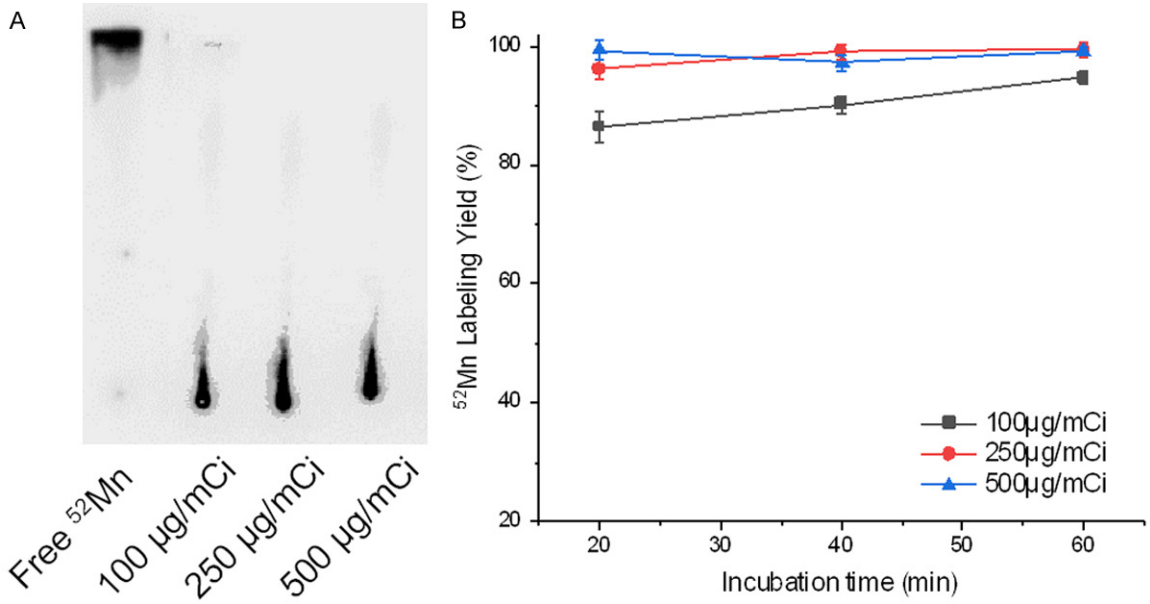

Figure S1. Radiolabeling study. A. Thin-layer chromatography at 60 min of incubation time. B. ^{52}Mn labeling yields as a function of incubation time and concentration of DOTA-YY146 per mCi of ^{52}Mn.

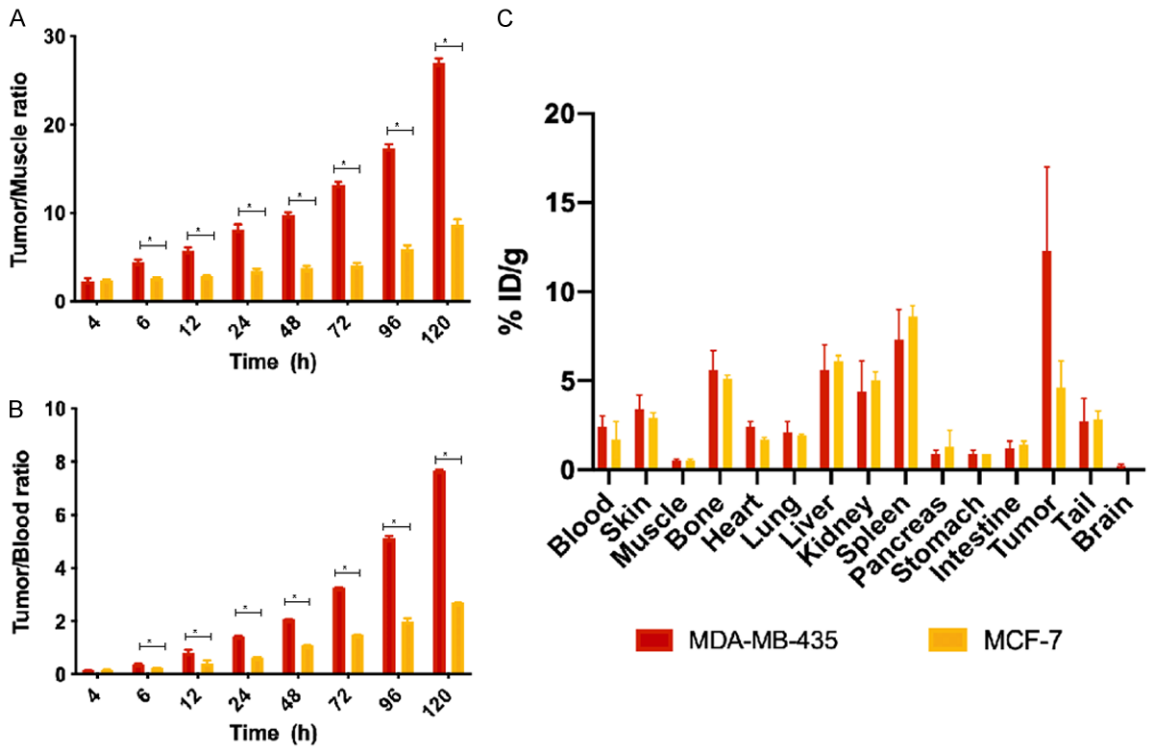

Figure S2. PET ROI analysis and biodistribution data. (A) Tumor-to-muscle and (B) Tumor-to-blood ratios based on the quantitative data obtained from analysis of PET images. *P < 0.05. (C) Ex vivo gamma counting biodistribution at 120 h post-injection of ^{89}Zr-Df-YY146 in mice bearing MDA-MB-435 or MCF-7 tumors.

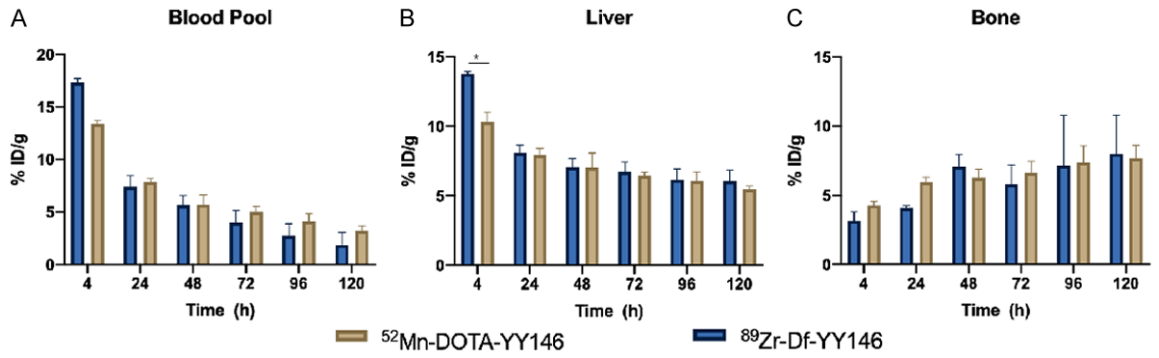

Figure S3. Direct comparison of tracer uptake between YY146 radiolabeled with ^{52}Mn or ^{89}Zr. Comparison between uptake in (A) Blood Pool, (B) Liver and (C) Bone after administration of ^{52}Mn-DOTA-YY146 or ^{89}Zr-Df-YY146 in animals bearing MDA-MB-435 tumors.

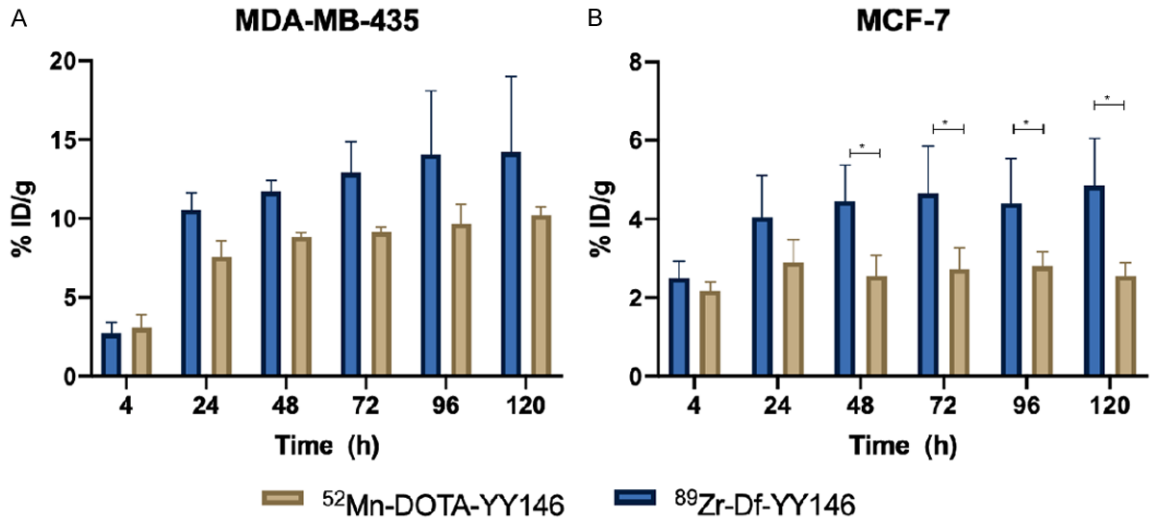

Figure S4. Differential uptake in the tumor. Comparison between tumor uptake of animals bearing (A) MDA-MB-435 and (B) MCF-7 tumors after administration of ^{52}Mn-DOTA-YY146 or ^{89}Zr-Df-YY146.

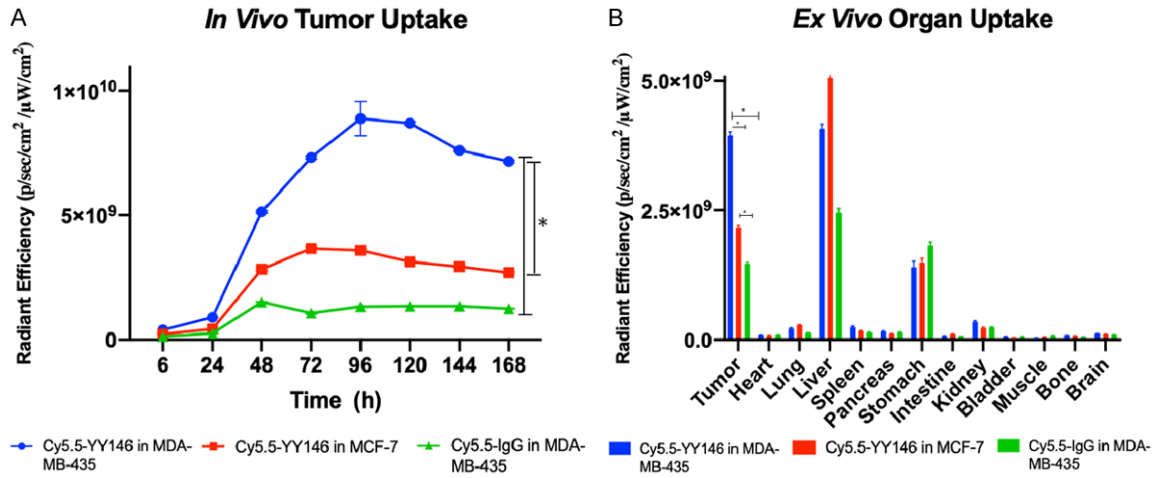

Figure S5. Semi-quantitative data from IVIS Imaging. A. *In vivo* ROI analysis of tumor uptake showing significantly higher tumor uptake in the MDA-MB-435 tumor bearing mice injected with Cy5.5-YY146 than all the other groups starting from 24 h p.i. until the end of the study. B. *Ex Vivo* ROI analysis of different organ uptakes among different groups. *P < 0.05.